

Influence of Graphite Addition on the Reactivity of Ti Powder with H₂ under Ball Milling

C. Borchers,^{*,†} T. I. Khomenko,[‡] O. S. Morozova,[‡] A. V. Galakhov,[§] E. Z. Kurmaev,[§]
J. McNaughton,[⊥] M. V. Yabloskikh,^{§,⊥} and A. Moewes[⊥]

Institute of Material Physics, University of Göttingen, Göttingen, Germany, Chemical Department, Lomonosov Moscow State University, Moscow, Russia, Institute of Metal Physics, Russian Academy of Sciences, Yekaterinburg, Russia, Department of Physics and Engineering Physics, University of Saskatchewan, Saskatoon, Canada.

Received: August 11, 2005; In Final Form: October 6, 2005

The effect of graphite addition on the mechanism of hydrogen uptake by titanium during mechanochemical activation in hydrogen flow was studied using kinetic, structural, microscopic, and spectroscopic techniques. As was found, already a small graphite admixture of about 0.5 wt % changed the kinetics of mechanically induced H₂ sorption and significantly stimulated Ti–H₂ interaction. Two new types of occupation sites available for hydrogen were observed, which are characterized by low H₂ desorption temperatures: about 650 and 750 K instead of 1000 K.

1. Introduction

In the last years, metal hydrides have attracted great attention as perspective materials for hydrogen storage since hydrogen can be stored more safely and compactly in them than in its compressed or liquid forms. To suit the technology requirements, fast hydrogenation and dehydrogenation kinetics at low temperatures together with high hydrogen capacity should be realized. Among the metals that form hydrides, Mg and Ti are known as the most lightweight materials; however, they are usually covered with thin layers of oxides or hydroxides and require activation treatment under high temperature (>300 °C) and hydrogen pressure (> 3MPa) before being used for storage and transport applications. A number of publications describe different methods designed to ease the activation processes.^{1–11} Ball milling of magnesium hydride powder together with various catalysts was studied by Oelerich and co-workers.⁴ They compared the catalytic effect of V₂O₅, VN, VC, and metallic V on the desorption kinetics of MgH₂ and found that the compounds mentioned above considerably enhance hydrogen sorption/desorption, whereas the catalytic effect of pure metals is less pronounced. The mechanism of the catalysis of the compounds is not well understood to date, but there are some hints that surface effects play a major role.^{4,12–15} It is supposed that graphite gives the highest sorption rate due to the formation of protective layers around the metal particles forming a barrier for oxidation.⁸ Moreover, it has been shown that graphite addition to ball milled TiH₂ powder significantly reduces the temperature of Ti–hydride decomposition due to Ti–C local bond formation.¹⁶

In previous works, the effect of graphite addition during the mechanical activation of TiH₂¹⁶ as well as the effect of graphite addition on hydrogen sorption properties of Ti after ball milling^{15,17} were studied. In this work, we study the effect of graphite addition on the mechanism of hydrogen uptake by

titanium during mechanochemical activation in hydrogen flow. We apply kinetic, structural, microscopic, and spectroscopic techniques. The chemical state and local structure of titanium and carbon atoms is analyzed by soft X-ray emission spectroscopy (XES), which is a local probe of the electronic structure of materials. With these studies we expect to find a highly porous nanocomposite material consisting of a microporous matrix of graphite and an active component Ti with high reactivity toward hydrogen. The findings of these studies are expected to provide a deeper understanding of the physical and chemical processes leading to this improvement.

2. Experimental Section

Starting powders were elemental titanium with a purity of 99.5% consisting of spherical particles of about 250 μm in diameter and highly oriented pyrolytic graphite (HOPG) with a purity of 99.0% and surface area $S = 3 \text{ m}^2/\text{g}$. The following experimental techniques were used: (1) Ball milling under flow conditions, where the flow gas was a mixture of He and 64 vol % H₂ at a flow rate of 8–10 mL/min, (2) Specific surface area measurement using low-temperature Ar adsorption (Brunauer–Emmett–Teller (BET) method), (3) X-ray diffraction, (4) scanning and transmission electron microscopy (SEM and TEM, respectively), and (5) temperature-programmed desorption and reaction (TPD and TPR, respectively). Details of these experimental methods are published elsewhere.¹⁵

Soft X-ray fluorescence was recorded as XES at beamline 8.0.1 of the Advanced Light Source at Lawrence Berkeley National Laboratory. The Ti Lα 3d_{4s} → 2p_{1/2} transition, Ti Lβ 3d_{4s} → 2p_{3/2} transition, and C Kα 2p → 1s transition were probed. XES were recorded at room temperature. Spectra were recorded for samples 2 and 3 and, as reference samples, pure Ti, TiH₂, TiC, HOPG, carbon fibers, as well as CH₃COCH₃, C₂H₅COCH₃, and C₂H₅COOH. To evaluate the emission spectra and to identify the phases present, we calculated the density of states (DOS) of Ti, TiH₂, and Ti₈H₁₆C₂, using the local density approximation (LDA) within the tight-binding linear Muffin–Tin orbitals (TB-LMTO) in atomic spheres approach. A model structure was used for TiH₂C_x calculations. It was built first by

* Corresponding author. E-mail: chris@ump.gwdg.de.

[†] University of Göttingen.

[‡] Lomonosov Moscow State University.

[§] Russian Academy of Sciences.

[⊥] University of Saskatchewan.

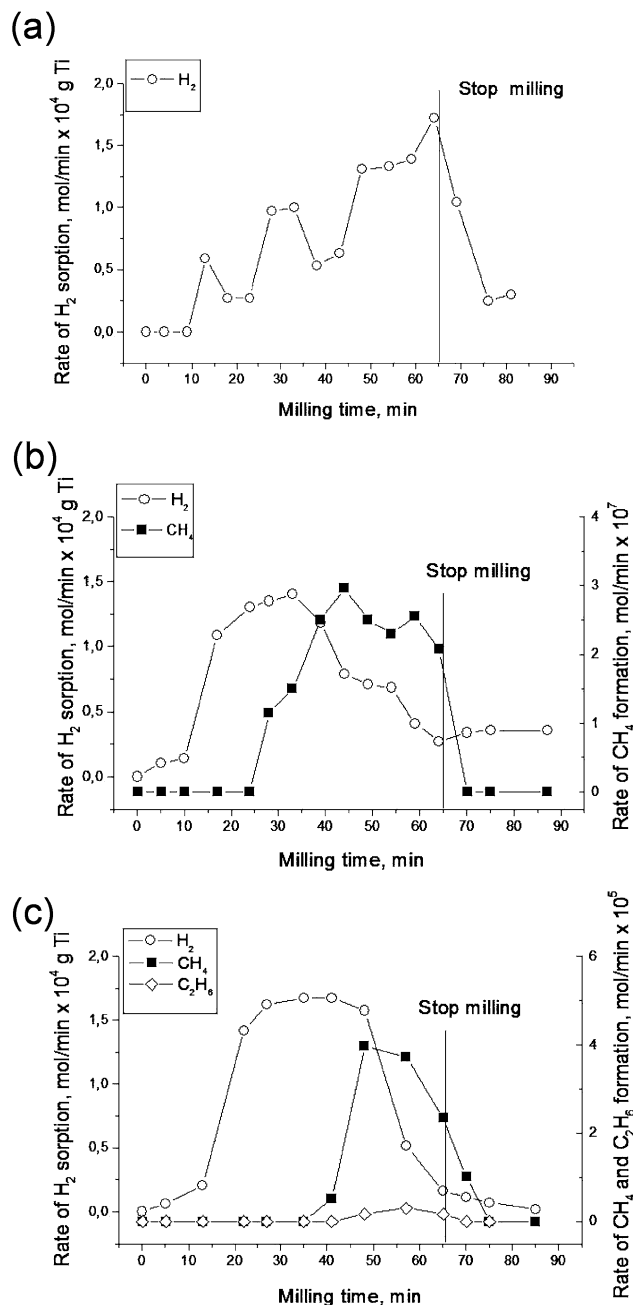


Figure 1. Kinetics of Ti-H₂ interaction under mechanical activation for (a) sample 1, (b) sample 2, and (c) sample 3.

doubling the unit cell of the cubic face-centered TiH₂ lattice along all three translation vectors resulting in 8 formula units per unit cell structure Ti₈H₁₆, and then adding carbon atoms into some empty octahedral positions. The rest of the octahedral positions were filled with empty spheres as needed for a TB-LMTO calculation. Two of such calculations were performed: one for pure Ti₈H₁₆, and one with two carbon atoms in the (0,0,0) and (1/2,1/2,1/2) positions, corresponding to Ti₈H₁₆C₂.

3. Results

3.1. Kinetics of Ti-H₂ Interaction under Mechanical Activation. The Figure 1 shows kinetic curves of hydrogen uptake during the milling of Ti and Ti/C powders: panels a, b, and c correspond to samples 1, 2, and 3, respectively. The pure Ti powder exhibits a steplike kinetic curve upon hydrogen absorption, see Figure 1a, with an incubation period of 10 min. An overall composition with a hydrogen-to-metal ratio H/Ti =

TABLE 1: H₂ Sorption and Hydrocarbon Evolution during Milling, and H Content after Milling

sample	composition	H ₂ uptake [mol]	CH ₄ & C ₂ H ₆ evolution [mol]	H content [H/Ti]
1	Ti	5.94×10^{-3}	8.5×10^{-6} (CH ₄)	0.32
2	Ti-0.5 wt % C	1.04×10^{-2}	7.6×10^{-4} (CH ₄)	0.55
3	Ti-16.0 wt % C	1.09×10^{-2}	4.5×10^{-5} (C ₂ H ₆)	0.59

0.3 was reached after 66 min of mechanochemical activation. Graphite addition changes the hydrogen sorption kinetics drastically. It stimulates H₂ uptake during the first 35–40 min of treatment (see Figure 1b,c). The process starts without any incubation period and slows down after 40–50 min of milling for both samples. In both cases, the process proceeds slowly in the first 10 min, takes up speed considerably in the next five min, and then slows down again. Parallel to this, CH₄ and C₂H₆ were detected after the peak of hydrogen uptake was reached. The rate of CH₄ and C₂H₆ formation was about 2 orders of magnitude higher for sample 3. After balancing the hydrogen uptake with the CH₄ and C₂H₆ evolution, the similar overall hydrogen contents of H/Ti = 0.55 (sample 2) and H/Ti = 0.59 (sample 3) were reached by Ti/C systems with quite different graphite contents (sample 2: 0.5 wt % C; sample 3: 16.0 wt % C). The parameters of the Ti-H₂ interaction are listed in Table 1.

3.2. Structure of As-Milled Powders. Figure 2a shows XRD patterns of the original and as-milled Ti and Ti/C powders. The original Ti powder (curve a) consists of hexagonal close-packed (hcp) αTi with lattice parameters $a = 0.295$ nm and $c = 0.469$ nm. The as-milled Ti powder, sample 1, (curve b) contains αTi and a titanium hydride. All Ti peaks are broadened, but there is no peak shift, compared to the original. A peak shape analysis reveals that the peak broadening is due to high strain and defect concentration. The phase of titanium hydride was identified as the tetragonal εTiH₂ phase with $a = 0.313$ nm and $c = 0.436$ nm (JCPDS 9-371). There are also αFe peaks, which correspond to ~2 wt % of Fe contamination. The content of metallic Ti was by quantitative phase analysis established as ~75 wt %. The hydrogen content in εTiH₂ was calculated on the basis of mass balance and quantitative phase analysis as H/Ti = 1.25.

The XRD pattern of sample 2 (curve c) is very similar to that of the as-milled Ti powder: they have the same positions of broad αTi peaks and peaks attributed to titanium hydrides. The hydrides were identified as a combination of tetragonal εTiH₂ phase with $a = 0.312$ nm, $c = 0.440$ nm (JCPDS 9-371) and cubic δTiH₂ with $a = 0.442$ nm (JCPDS 25-982). There are also αFe peaks, which correspond to ~1 wt % of Fe contamination. No peaks of C, Ti-C, or Ti-C-H phases were detected. The content of metallic Ti was established as ~55 wt %. The hydrogen content in δTiH₂ and εTiH₂ was calculated as H/Ti ≈ 1.2, but, from this analysis, it is impossible to tell how much hydrogen is in each one of these phases.

The XRD pattern of sample 3 (curve d) contains peaks attributed to C, αTi, and Ti hydride or a combination of Ti hydride and Ti carbide phases. The half-width and positions of the αTi peaks are very similar to those observed for sample 2. Extremely broad peaks correspond to εTiH₂ or to a combination of εTiH₂ and cubic TiC ($a = 0.431$ nm) (JCPDS 31-1400). The presence of TiC was proposed because this phase was identified in the XRD pattern of sample 3 after TPD (Figure 2b, curve d-1) in an amount of ~20 wt % together with αTi with enlarged lattice parameters ($a = 0.295$ nm, $c = 0.470$ nm). Because of this, the phase composition of sample 3 was not estimated

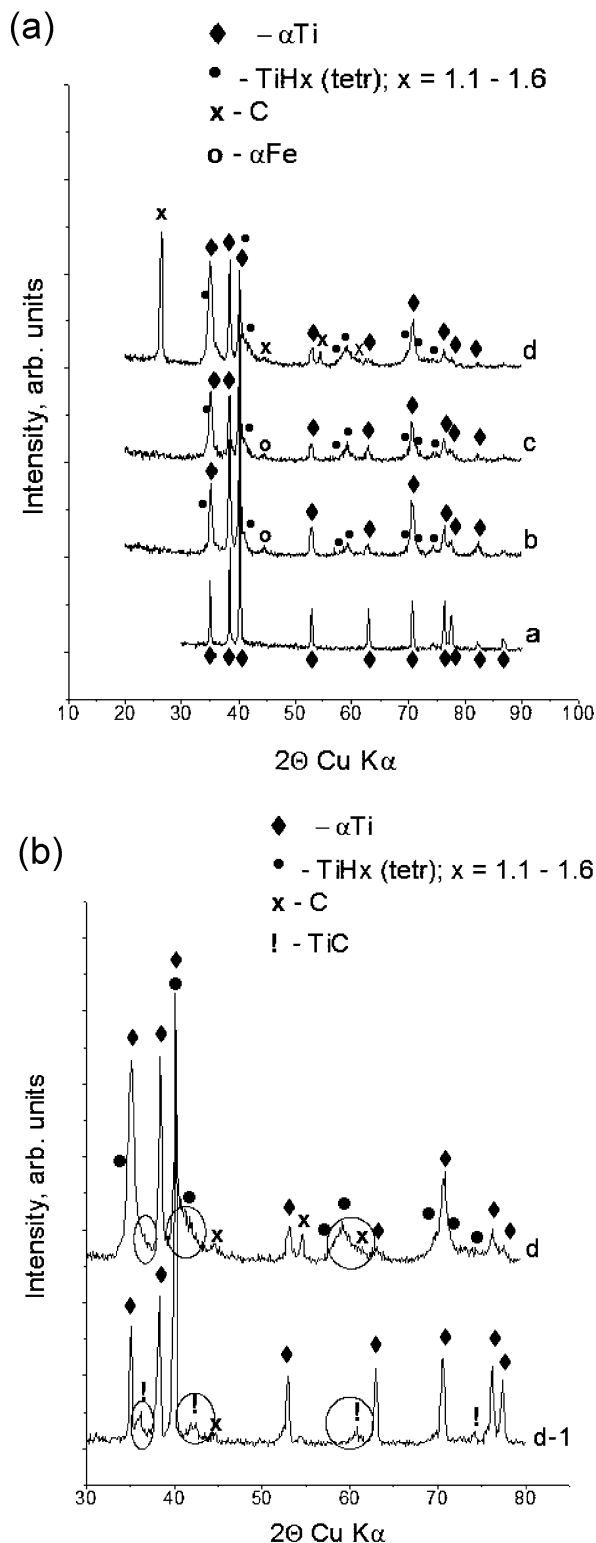


Figure 2. XRD patterns of (a) original Ti powder and samples 1–3. Curve a: original Ti; curve b: sample 1; curve c: sample 2; curve d: sample 3. (b) Sample 3 as-prepared and after TPD. Curve d: sample 3 as-prepared; curve d-1: sample 3 after TPD.

numerically (see Table 2). No α Fe contamination was detected in this sample.

Structure, phase composition, and lattice parameters of as-milled Ti and Ti/C powders are given in Table 2.

3.3. Morphology and Microstructure of As-Milled Powders. The morphologies of original Ti and as-milled Ti and Ti/C powders are shown in the SEM micrographs in Figure 3. The

TABLE 2: Structure and Phase Compositions of Ti and Ti/C Powders

sample	phase	structure ^a	lattice constants [nm]	fraction [wt %]
original	α Ti	hex	$a = 0.295$; $c = 0.469$	100
1	α Ti	hex	$a = 0.295$; $c = 0.469$	75
	ϵ TiH ₂	tetr	$a = 0.313$; $c = 0.436$	23
	α Fe			2
2	α Ti	hex	$a = 0.295$; $c = 0.469$	55
	δ TiH ₂	cub	$a = 0.442$	37
	ϵ TiH ₂	tetr	$a = 0.312$; $c = 0.440$	11
	α Fe			1
3	α Ti	hex	$a = 0.295$; $c = 0.469$	
	ϵ TiH ₂	tetr	$a = 0.315$; $c = 0.439$	
	TiC or Ti(C,H)	cub	$a = 0.432$	
	C			

^a Hex = hexagonal; tetr = tetragonal; cub = cubic.

original Ti powder (specific surface area $S = 0.02 \text{ m}^2/\text{g}$) consists of spherical particles of narrow size distribution ($d \approx 250 \mu\text{m}$). The Figure 3b,c shows that samples 1 and 2 have a similar heterogeneous morphology. Both samples consist of deformed and flat particles ($150\text{--}300 \mu\text{m}$ in size) with rough surface and several platelets. Simultaneously, a fraction of small particles with average size of about $5\text{--}20 \mu\text{m}$ is present. This fraction is most likely to be a Ti hydride-rich powder formed as a result of hydrogen embrittlement. The difference between the sample morphology is in a relationship between small and large particle fractions: sample 2 contains a larger fraction of small particles compared to sample 1. The specific surface area of these samples is considerably larger than that of original Ti powder: $S = 1.6 \text{ m}^2/\text{g}$ for sample 1, and $S = 1.8 \text{ m}^2/\text{g}$ for sample 2.

Figure 3d shows a significant change in morphology for sample 3, containing thirty times as much graphite as sample 2. The major part of the powder consists of platelets from 10 to $200 \mu\text{m}$ in size. The smallest particles stick together to create agglomerates of $5\text{--}10 \mu\text{m}$ in size. Only a few large deformed particles can be seen. The specific surface area of this sample is $S = 14.8 \text{ m}^2/\text{g}$.

The microstructure of as-milled powders was studied by TEM. Figure 4 shows the microstructure of sample 2. One can see a Ti particle, appearing dark, covered by a thin layer of carbon, recognizable by the wavy rim of the particle. The particle size is larger than 300 nm . The light structure in the lower right of the micrograph is a filament of the supporting carbon. Figure 5 shows the microstructure of sample 3. In Figure 5a, an overview can be seen. The metal and/or hydride particles appear dark. A bimodal particle distribution can be seen: on one hand, nanometer-sized particles are embedded in a carbon matrix, on the other hand, fairly large particles, several tens of nanometers large, are covered with a thin carbon shell. In Figure 5b, details of the carbon matrix are shown. At the right, there is a crystalline carbon nanorod; the rest of the carbon in this micrograph is amorphous, exhibiting spongy and filamental structures. The dark spots on the left side are metal or hydride particles embedded in the amorphous matrix. Thus, a trimodal particle-size distribution is revealed: particles in the $10\text{--}200 \mu\text{m}$ range, as can be seen in the SEM micrograph in Figure 3d, particles in the range of $30\text{--}300 \text{ nm}$, and particles with a size well below 10 nm . The latter particles are always embedded in a carbon matrix, while the first and second categories are covered by a thin carbon layer.

3.4. TPD from Mechanically Activated Powders. Panels a, b, and c of Figure 6 show the TPD spectra for samples 1, 2, and 3, respectively. A single-peak TPD curve ($T_{\text{max}} = 1000 \text{ K}$) was observed for sample 1 (Figure 6a). A drastic change in the

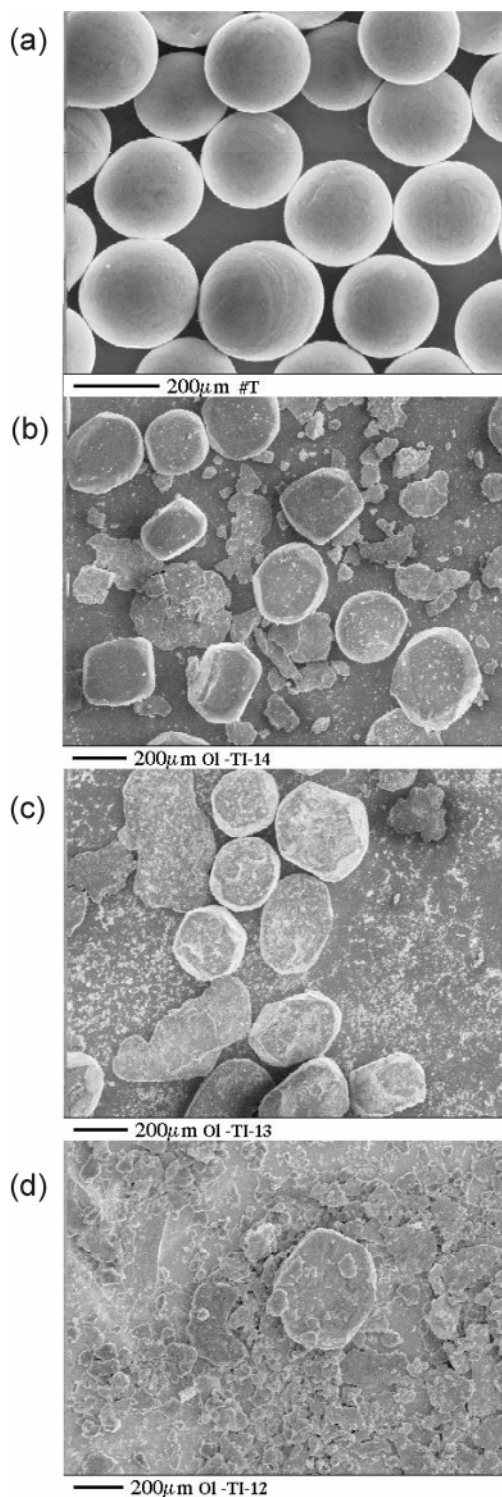


Figure 3. SEM micrographs of (a) original Ti powder, (b) sample 1, (c) sample 2, and (d) sample 3.

TPD spectra was observed for the milled Ti/C powders compared to that of pure Ti powder. The TPD curves exhibit three peaks with a high-temperature peak at 910 K (Figure 6b,c). Approximately 84 mol % for sample 2 and 63 mol % for sample 3 of total H_2 is localized in these positions. Two other TPD peaks at ~ 650 and ~ 750 K can be observed for Ti/graphite powders.

After milling, another portion of samples 2 and 3 was subjected to a TPR treatment after mechanical activation under hydrogen flow, to see if the sites available for hydrogen were saturated under ball milling. The result can be seen in Figure

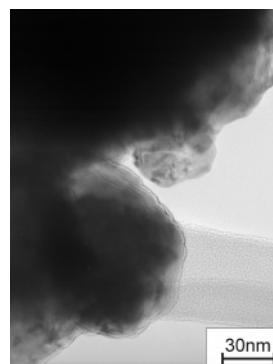


Figure 4. TEM micrograph of sample 2. A Ti particle, appearing dark, is covered by a thin layer of carbon, recognizable by the wavy rim of the particle. The particle size is larger than 300 nm. The light structure in the lower right of the micrograph is a filament of the supporting carbon.

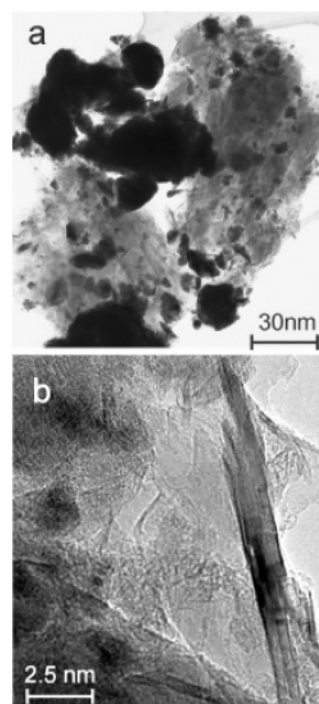


Figure 5. TEM micrographs of sample 3. (a) The metal and/or hydride particles appear dark. A bimodal particle distribution can be seen: on one hand, nanometer-sized particles are embedded in a carbon matrix; on the other hand, fairly large particles, several tens of nanometers large, are covered with a thin carbon shell. (b) Details of the carbon matrix. At the right, there is a crystalline carbon nanorod; the rest of the carbon in this micrograph is amorphous, exhibiting spongy and filamental structures. The dark spots on the left side are metal or hydride particles embedded in the amorphous matrix.

7a. Both samples exhibit a two-peak spectrum, with the maximum absorption rate on the high-temperature peak at 822 K for sample 2 and 724 K for sample 3. The lower peak of each of the samples is situated about 80 K lower in both cases. To study the stability of the low-temperature sites, a series of TPD–TPR–TPD experiments was carried out. Figure 7b illustrates results obtained for sample 2. The first heating (TPD, curve 1) is the same as that shown in Figure 6b, only reversed. The next TPR with H_2 exhibits only two peaks at ~ 770 and ~ 910 K (curve 2). This reduces the total hydrogen capacity by approximately 30%. The TPD spectrum recorded after this reaction consists of a single narrow peak at ~ 921 K (curve 3).

3.5. Soft XES. Figure 8a shows the results of measurements of Ti $L\alpha$ and Ti $L\beta$ XES of samples 2 and 3 and the reference

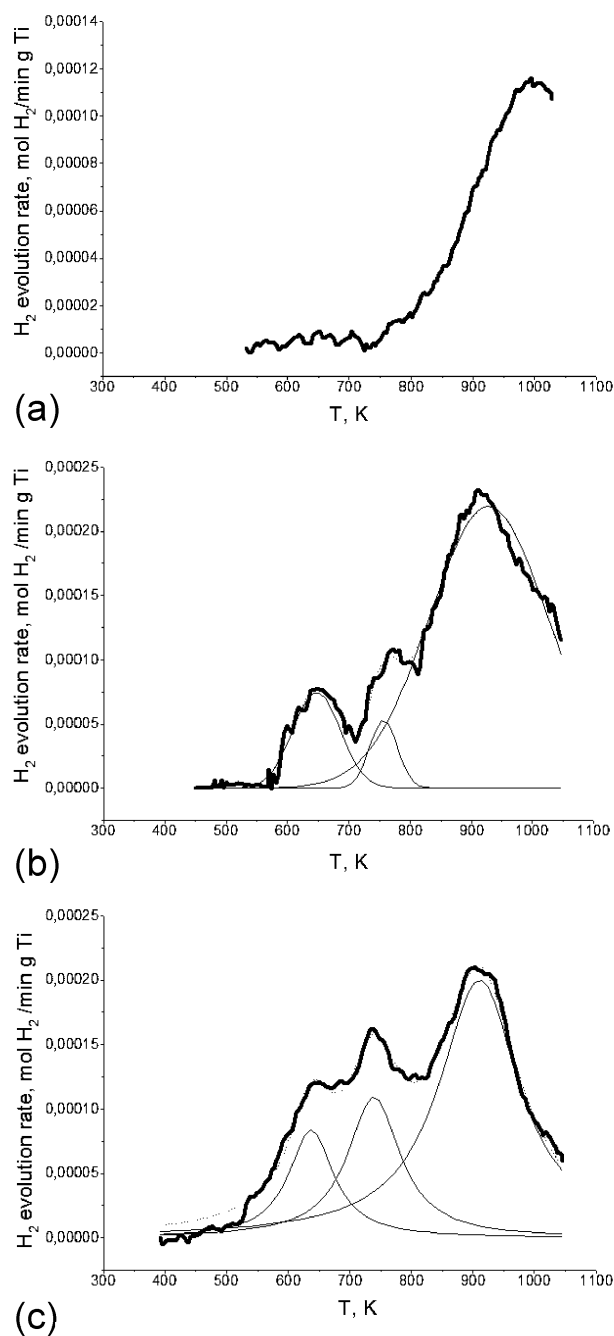


Figure 6. TPD spectra for (a) sample 1, (b) sample 2, and (c) sample 3.

samples Ti-metal and TiH_2 . One can find in the Ti $L\alpha$ XES of samples 2 and 3 an additional subband B, which is absent in the spectrum of pure Ti. The energy location of this subband with respect to that of the main band A is found to be the same as that in TiH_2 (see Figure 8a), and its relative intensity $I(B)/I(A)$ is higher in sample 2 than it is in sample 3 but still lower than it is in pure TiH_2 . Figure 8b shows the results of TB-LMTO electronic structure calculations, according to which the total DOS of TiH_2 shows an essential difference with respect to that of pure metallic Ti. In the TiH_2 below the metal d -bands, the metal–hydrogen-derived states with a total width of 8 eV are present on the low-energy side of the energy spectrum. The results of our calculations are in a good agreement with those of other groups.^{18–21}

Figure 9 shows the TB-LMTO analysis of a situation in which carbon occupies the octahedral interstitials in TiH_2 lattice. Figure 9a shows the total DOS, 9b shows the Ti DOS, 9c shows the H

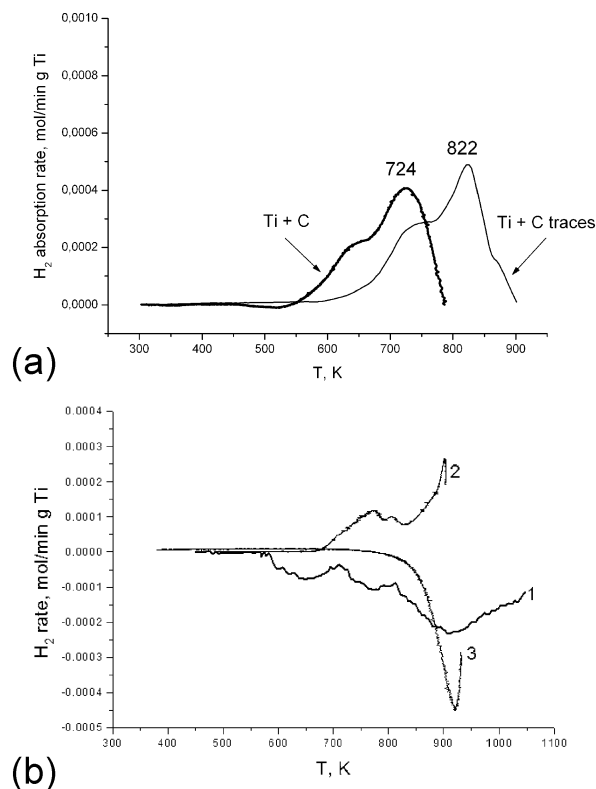


Figure 7. (a) TPR performed on samples 2 (marked Ti + C traces) and 3 (marked Ti + C) after milling for 60 min in hydrogen flow. (b) TPD and TPR spectra for sample 2. Curve 1: TPD after milling; curve 2: TPR after TPD; curve 3: TPD after TPD and TPR.

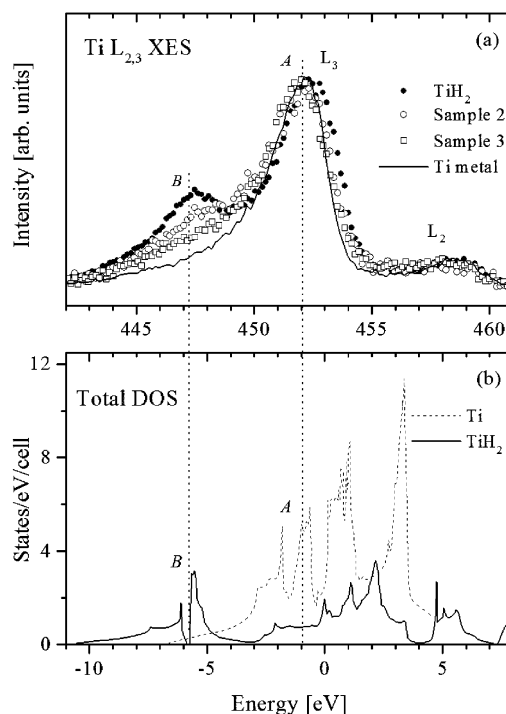


Figure 8. (a) Ti $L\alpha$ and Ti $L\beta$ XES of samples 2 and 3 and the reference samples of Ti-metal and TiH_2 . (b) TB-LMTO electronic structure calculations, of which the total DOS is shown for Ti and TiH_2 .

1s DOS, and 9d shows the C $2p$ and C $2s$ DOS. As can be seen in Figure 9(c), it is found that the occupation of octahedral interstitials by carbon atoms blocks the formation of titanium–hydrogen bonds, and the amount of bonded hydrogen is decreased.

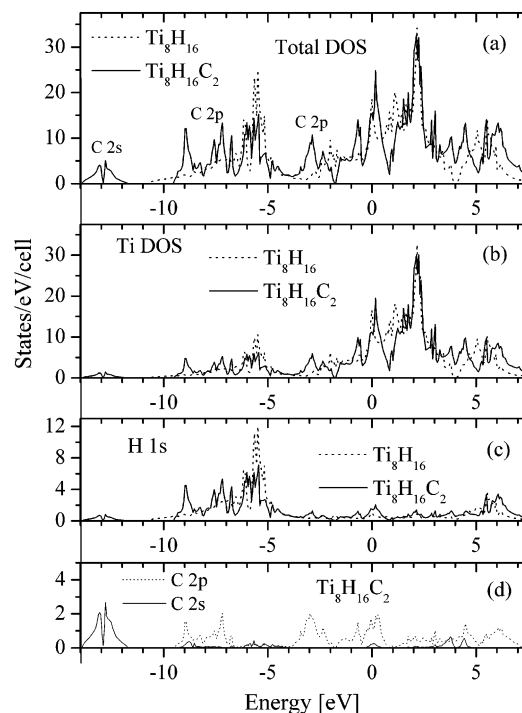


Figure 9. TB-LMTO analysis of a situation in which carbon occupies the octahedral interstitials in TiH_2 lattice. (a) Total DOS, (b) Ti DOS, (c) H 1s DOS, and (d) C 2p and C 2s DOS.

Figure 10 shows the C K α XES of samples 2 and 3, compared to those of the reference samples of TiC, HOPG, and carbon fibers as well as CH_3COCH_3 , $\text{C}_2\text{H}_5\text{COCH}_3$, and $\text{C}_2\text{H}_5\text{COOH}$. The C K α XES ($2p \rightarrow 1s$ transition) of samples 2 and 3 are found to be different from each other and are also not similar to the spectrum of HOPG (Figure 10a). The comparison of the C K α XES of sample 2 with the spectra of the reference samples of ketones and carboxylic acid (CH_3COCH_3 , $\text{C}_2\text{H}_5\text{COCH}_3$, and $\text{C}_2\text{H}_5\text{COOH}$) shows some correlation between the highest energy position of the spectra, but the agreement with the spectra of the reference samples is not full (Figure 10b). On the other hand, we found that a comparison of the C K α XES of sample 2 with the spectra of the reference samples of TiC and HOPG shows a good correspondence with the superposition of 50% TiC and 50% HOPG (see Figure 10c). Figure 10d shows that the C K α XES of sample 3 is similar to the spectrum of carbon fiber with the addition of 10% TiC (Figure 10c).

4. Discussion

Graphite addition and ball milling significantly improve the reactivity of Ti toward hydrogen by modifying some characteristics of the original powder. The Fe peaks observed in pure Ti are due to dry operation with stainless steel balls, while the missing peaks in the Ti–16 wt % C powders are due to wet operation in the presence of graphite. In sample 2, the amount of graphite was not sufficient for complete wetting. No Ti–Fe intermetallic phases are observed, so a possible stimulating effect of Fe on hydrogen sorption–desorption properties are taken to be negligible, particularly since Fe has, contrary to Ti, a positive heat of mixing with H.²²

The observed stepwise uptake of hydrogen in the carbon-free sample 1 (see Figure 1a), is typical for a diffusion-controlled process. As titanium hydride surface layers on the Ti particles are formed, they may suppress further Ti–H₂ interaction. With continuous ball milling, the hydride layers are eventually smashed, and further hydride formation can take place. As the

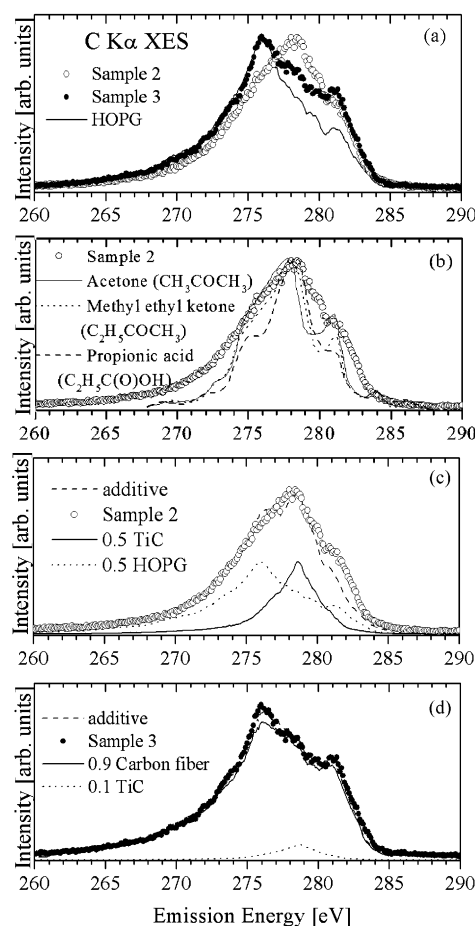


Figure 10. C K α XES of samples 2 and 3, compared to those of the reference samples (a) HOPG, (b) CH_3COCH_3 , $\text{C}_2\text{H}_5\text{COCH}_3$, and $\text{C}_2\text{H}_5\text{COOH}$, (c) 50% TiC and 50% HOPG, and (d) 90% carbon fibers and 10% TiC.

average particle size decreases, the peak height of H₂ sorption can rise. The observed incubation period is most probably due to the fact that the native oxide surfaces of the Ti powder particles have to be broken up before a noticeable Ti–H reaction can take place.

As soon as carbon comes into the game, the picture is quite different (see Figure 1b,c). The incubation period is missing, but, during the first 10 min, the hydrogen uptake is rather sluggish. Native oxides are present in samples 2 and 3 as well, but obviously the carbon can protect the fresh metallic surfaces from renewed oxidation to an extent that is not possible when Ti is milled without graphite. The stepwise uptake of hydrogen is replaced by a continuous uptake, which starts without an incubation period and, after a plateau period, decreases substantially before the milling is ended and before the samples are saturated with hydrogen.

After milling, the H/Ti fraction is about 0.5 in samples 2 and 3, whereas H/Ti is about 0.3 in sample 1. Methane and, to a lesser extent, ethane formation is observed for the carbon containing phases: about 1% of the carbon in sample 2 and 3% in sample 3 are active enough to form hydrocarbons. McCarty and Wise studied the hydrogenation of surface carbon on alumina-supported nickel.²³ They found three different carbon species: a highly reactive adatom species α' that can react with H₂ to form CH₄, a chemisorbed species α that eventually triggers carbide formation, and a surface-carbon phase β that can have a filamental or a more graphite-like structure. All of these species show different reaction temperatures with hydrogen to form methane.²³ Although the interaction of Ni with C and H

cannot be compared with that of Ti with C and H, the formation of different carbon species is highly probable in the ball milling of C with Ti as well. Carbon species such as those called β by McCarty and Wise²³ are obviously present, as can be seen in the TEM micrograph in Figure 5b.

In the case of the Ni–C–H system, metal hydride formation is improbable since the enthalpy of mixing of H in Ni is positive.²² For the Ti–C–H system, TiC formation is most probable from the point of view of equilibrium enthalpies: $H(\text{TiC}) = -92.26 \text{ kJ/g}\cdot\text{atom}$, $H(\text{TiH}_2) = -48.12 \text{ kJ/g}\cdot\text{atom}$, and $H(\text{CH}_4) = -14.97 \text{ kJ/g}\cdot\text{atom}$.²⁴ But, since solid–vapor interaction is much faster than solid–solid interaction, metal hydride formation is kinetically favored in the early stages and low-temperature regimes of the interaction. Methane formation will only be observed when a highly reactive carbon species such as α' in the notation of McCarty and Wise is present. In this work, we observed 1–3% of this species.

TPD shows a single-peak curve ($T_{\text{max}} = 1000 \text{ K}$) for graphite-free sample 1 (Figure 6a) and high-temperature peaks at 910 K for samples 2 and 3. In a previous work, Ti and a Ti–16 wt % C mixture were ball milled in He atmosphere and subsequently loaded with hydrogen.¹⁵ The TPR and TPD peaks were located at 840 and 900 K, respectively. For the Ti/C mixture, the high-temperature TPR peak was found at $\sim 700 \text{ K}$, and the TPD peak was found at $\sim 800 \text{ K}$.¹⁵ Apparently, graphite addition shifts the peak positions to lower temperatures. A reason for this can be that the graphite keeps the Ti from agglomerating, so particle size is extremely small, which in turn can enhance desorption kinetics.

These highest peaks are in good agreement with the highest peak at $\sim 820 \text{ K}$ in the TPD spectrum of TiH_2 shown in a previous work.¹⁶ This peak can be attributed to the occupation sites in titanium bulk. However, standard TiH_2 exhibits a very sharp desorption peak with a half-width of $\sim 80 \text{ K}$,¹⁶ while the peak observed in this work has a half-width of $\sim 190 \text{ K}$. This indicates that one type of site with a continuous site energy distribution gets occupied by H atoms in the Ti bulk lattice under milling. H atoms randomly occupy tetrahedral interstitial sites with the same energy in an undisturbed Ti lattice.²² However, as was shown for hydrogen-containing disordered or amorphous alloys,^{22,25–27} there may be different types of sites with a distribution in chemical as well as geometrical configuration, leading to a distribution of site energies for the H atoms. This manifests itself in a broadening of the TPR (or TPD) peaks.

Two other TPD peaks at ~ 650 and $\sim 750 \text{ K}$ observed for Ti/C powders show that two additional discrete types of sites are available for hydrogen under milling with graphite. When a Ti–16 wt % C mixture is ball milled in He atmosphere and subsequently loaded with hydrogen during TPR,¹⁵ two additional peaks are also observed at 525 and 600 K. If one compares the TPR curves of samples 2 and 3 reacted to saturation after milling (Figure 7a), it catches one's eye that the low-temperature peak is missing, while the other two peaks occur in both samples. These peaks correspond to the high-temperature bulk sites (822 K for sample 2 and 724 K for sample 3) and to the peaks at intermediate temperatures in TPD after milling under H_2 flow. Obviously, the major part of the hydrogen uptake during ball milling goes into the sites represented by the low-temperature peak, and only a small amount goes into the high-temperature bulk peak. In addition, the low-temperature site is saturated with hydrogen after milling.

When we compare these results with those of McCarty and Wise,²³ it is obvious that, in both cases, three types of carbon are present. Each of these types promotes a different reaction

of hydrogen. It should be kept in mind though, that, because of the different metals present, the reaction temperatures do not necessarily coincide with those observed by McCarty and Wise. The filamental or graphitic carbon species β act as a matrix-forming agent and protect the metal particles from sticking and oxidation. During milling, it can enhance hydrogen transportation to the Ti particles. The first two steps of the reaction of hydrogen with metals are physisorption and chemisorption. Physisorption of H_2 is enhanced by carbon, especially when it is nanoporous or filamental like species β .^{28–30} On the other hand, the dissociation of H_2 and subsequent chemisorption is greatly enhanced by metals, especially in the presence of d -electrons,^{31,32} as is the case for Ti. The combination of these two effects most probably leads to the pronounced maximum in hydrogen uptake, reflected by the TPD peak at $\sim 650 \text{ K}$ (see Figure 6). The corresponding sites are saturated after 40–50 min of milling. Yildirim and Ciraci³⁴ report about using titanium-decorated nanotubes as a hydrogen storage medium, and Zhao et al. report about hydrogen storage in transition-metal-decorated buckyballs.³⁵ The latter group states that binding energies are significantly higher than simple physisorption and substantially lower than if atomic hydrogen were chemisorbed on the metal surfaces.³⁵ The first pair calculated the DOS of one Ti molecule, four H_2 molecules, and one hexagon of carbon on which Ti and H_2 molecules are bonded.³⁴ They found that the binding state just below the Fermi level E_F has a major contribution from the Ti d orbitals, together with the carbon p orbitals and hydrogen s orbitals. From their results, it is clear that the carbon atoms are involved in the bonding of hydrogen to Ti. One can assume that, in our case, the carbon species β with graphitic structure plays a role in this process. This is corroborated by the results of XES (see Figure 10c). The C K α of sample 2 can be fitted nicely by a mixture of HOPG and TiC. In this sample, most of the carbon is in close contact with Ti particles, which makes C K α meaningful with regard to C–Ti interaction.

This kind of binding is a pure surface effect and is just as pronounced with 0.5% C (sample 2) as it is with 16.0 wt % C (sample 3), whereas the peak at $\sim 750 \text{ K}$ is much smaller for the sample with only traces of C. Here, the C atoms of species α chemisorbed on the surface or subsurface sites of Ti play a major role. The C atoms are known to occupy octahedral positions,³³ disturbing the neighbor tetrahedral positions suitable for H atoms, as the TB-LMTO results have shown (see Figure 9). According to Blanter and co-workers,²⁵ in the body-centered cubic (bcc) α -Ti lattice, H atoms experience a strong attraction in the second shell around C atoms, whereas the first shell is blocked. The fact that no change was observed in the lattice constants of Ti after the milling with graphite indicates that no bulk Ti–C solid solution had formed under milling. Consequently, the above reactions are mainly subsurface reactions. This attractive reaction is quite distinct from the high-temperature bulk hydride formation, and merges into a distinct TPD peak at $\sim 750 \text{ K}$. The TiC in sample 2 mentioned above is most probably a subsurface solid solution of C in Ti.

Since under milling no bulk solid solution nor TiC is formed, hydrogen can diffuse into the Ti particles to form Ti hydride, desorbing in the high-temperature TPD bulk peak.

When Ti/C powder mixtures are milled in He flow and subsequently subjected to a TPR treatment with hydrogen, the low-temperature peak is also quite prominent.¹⁵ It is remarkable, though, that it is not observed in a subsequent desorption treatment, while it is seen in the desorption after milling of Ti/C powders in hydrogen flow. When the latter is subjected to a

second TPR, the low-temperature peak is gone, too. Obviously, the heating stimulates the chemisorbed carbon α to form a solid solution with Ti, as was found with XRD (see Figure 2b). The mechanical activation of structural and chemical transformations was also studied in the Zr–C–H system.³⁶ Here too, Zr and C were milled in hydrogen flow. In the first 80 min, the formation of ZrH₂ in a solid–gas reaction was observed, and, in the second stage, the formation of a Zr–C solid solution during the decomposition of ZrH₂ was observed. In this system, which is chemically similar to the Ti–C–H system, it was found that thermodynamically favorable carbide formation is initially suppressed for kinetic reasons but wins through after due time, even in persistent hydrogen flow.³⁶

The Ti L α,β XES (Ti L_{2,3} in Figure 8) correspond to the $3d4s \rightarrow 2p_{1/2,3/2}$ transition and probes the distribution of $3d4s$ occupied states. As seen, Ti L α,β consists of two bands, the energy difference of which corresponds to Ti $2p$ spin–orbit splitting. The low-energy band B corresponds to TiH₂. In TiH₂, below the metal d -bands, metal–hydrogen-derived states are present on the low-energy side of the energy spectrum. These states are due to an overlapping of metal–hydrogen bonding and hydrogen–hydrogen antibonding states, in which the metal–hydrogen interaction is responsible for the lowering of metal states to the bottom of the valence band. A DOS analysis into its partial wave components inside the hydrogen and titanium spheres (see Figure 8b), shows that the low-lying B bands are formed mainly by the hydrogen s -states and titanium d -states. It is therefore clear that the origin of the B band in the Ti L α,β XES of samples 2 and 3 is due to the formation of Ti–H bonds under mechanical activation in hydrogen flow.

Model band structure calculations of TiH₂–C system in which some tetrahedral sites of the host TiH₂ lattice of some tetrahedral sites by carbon atoms results in a reduction of DOS in the region of the B peak and a weakening of metal–hydrogen bonding. As stated above, carbon blocks the nearest-neighbor sites for hydrogen, which is confirmed by these results. When the carbon content is large enough for TiC to be formed, the carbide is blocked for hydrogen uptake altogether.^{15,36}

The C K α XES ($2p1s$ transition) of samples 2 and 3 are found to be different and are also not similar to the spectrum of HOPG (Figure 10a). The C K α XES of sample 3 is rather similar to those of carbon fiber with the addition of 10% C bonded to Ti (Figure 10d), a result which is corroborated by TEM results (see Figure 5b). The chemical state of carbon atoms for low content of graphite additive (sample 2) is found to be most difficult for analysis. The comparison of the C K α XES of sample 2 with the spectra of the reference samples of TiC and HOPG or ketones and carboxylic acid shows some correlation between the energy positions of spectral features; however, the agreement with the spectra of reference samples is not full (see Figure 10b,c). One should bear in mind, that the carbon content is quite low in this sample. One can assume that some of the carbon forms Ti–C bonds, most probably the species called α by McCarty and Wise. Some perhaps form COH fragments, perhaps the reactive species α' . The rest of the carbon, which is small for sample 2, belongs to the species β , which adopts the graphitical form. Sample 3 with more carbon contains a smaller proportion of Ti–C bonds because in sample 2, with only 0.56 wt % of C, a much higher proportion of the total carbon is in close contact with Ti. If COH fragments are present in sample 3, their amount is too small for detection in this sample. Here, the species β in its filamental form represents the largest amount of carbon. One can therefore assume that β

is rather graphitical near Ti surfaces and filamental where it is isolated.

5. Conclusions

Even a small graphite addition (0.5 wt %) changes the kinetics of mechanically induced H₂ uptake by Ti powder. Ti or Ti hydride particles covered by a graphite layer of 1–3 nm thickness are formed when Ti/C powder contains traces of graphite. A porous graphite matrix with randomly distributed Ti or Ti hydride fragments several nanometers in diameter is formed when the Ti/C powder contains 16 wt % of graphite. In both cases, new types of occupation sites available for hydrogen in Ti are observed. They are characterized by a drastic reduction of H₂ desorption temperature: from 1000 to 650 and 750 K, respectively. The hydrogen distribution between the site types significantly depends on the different types of carbon that are produced during the milling process. The first type of site with the lowest desorption temperature seems to be surface sites, where graphitic or filamental carbon plays a role in the binding of hydrogen to Ti. The second type of site with intermediate desorption temperature seems to belong to subsurface sites, where chemisorbed subsurface carbon attracts hydrogen to second-neighbor sites. The site with highest desorption temperature is the Ti bulk site.

Acknowledgment. We are thankful to Dr. A. N. Streletskii (Institute of Chemical Physics, RAS) for valuable comments and discussion, to Dr. H. Jander (Institute of Physical Chemistry, University of Göttingen) for the preparation of TEM samples, to A. B. Borunova (Institute of Chemical Physics, RAS) for the specific surface area measurements, and to A. V. Leonov (Chemical Department, Moscow State University) for XRD measurements. This work was partially supported by RFBR, project No 040332215, which is gratefully acknowledged.

References and Notes

- (1) Schlappbach, L. *Solid State Commun.* **1981**, *38*, 117.
- (2) Zhang, H.; Kisi, E. H. *J. Phys.: Condens. Matter* **1997**, *9*, L185.
- (3) Bouaricha, S.; Dodelet, J. P.; Guay, D.; Huot, J.; Boily, S.; Schulz, R. *J. Alloys Compd.* **2000**, *307*, 226.
- (4) Oelerich, W.; Klassen, T.; Bormann, R. *J. Alloys Compd.* **2001**, *32*, L5.
- (5) Dehouche, Z.; Klassen, T.; Oelerich, W.; Goyette, J.; Bose, T. K.; Schulz, R. *J. Alloys Compd.* **2002**, *347*, 319.
- (6) Sandrock, G.; Gross, K.; Thomas, G. *J. Alloys Compd.* **2002**, *339*, 199.
- (7) Janot, R.; Rougier, A.; Aymard, L.; Lenain, C.; Herrera-Urbina, R.; Nazri, G. A.; Tarascon, J. M. *J. Alloys Compd.* **2003**, *356–357*, 438.
- (8) Güvendiren, M.; Baybörü, E.; Öztürk, T. *Int. J. Hydrogen Energy* **2004**, *29*, 491.
- (9) Barkhordarian, G.; Klassen, T.; Bormann, R. *J. Alloys Compd.* **2004**, *364*, 262.
- (10) Mulana, F.; Nishimiya, N.; Saito, H.; Matsumoto, A.; Tsutsumi, K. *J. Alloys Compd.* **2004**, *372*, 245.
- (11) Kondo, T.; Shindo, K.; Sakurai, Y. *J. Alloys Compd.* **2005**, *386*, 202.
- (12) Dehouche, Z.; Goyette, J.; Bose, T. K.; Schulz, R. *Int. J. Hydrogen Energy* **2003**, *28*, 983.
- (13) Janot, R.; Aymard, L.; Rougier, A.; Nazri, G. A.; Tarascon, J. M. *J. Phys. Chem. Solids* **2004**, *65*, 529.
- (14) Hanada, N.; Ichikawa, T.; Fujii, H. *J. Phys. Chem B* **2005**, *109*, 7188.
- (15) Borchers, C.; Leonov, A. V.; Khomenko, T. I.; Morozova, O. S. *J. Phys. Chem B* **2005**, *109*, 10341.
- (16) Kurmaev, E. Z.; Morozova, O. S.; Khomenko, T.; Borchers, C.; Nemnonov, S. N.; Harada, Y.; Tokushima, T.; Osawa, H.; Takeuchi, T.; Shin, S. *J. Alloys Compd.* **2005**, *395*, 240.
- (17) Borchers, C.; Leonov, A. V.; Khomenko, T. I.; Morozova, O. S. *J. Mater. Sci.* **2003**, *39*, 5259.
- (18) Hygh, E. H.; Welch, R. M. *Phys. Rev. B* **1970**, *1*, 2424.
- (19) Jepsen, O. *Phys. Rev. B* **1975**, *12*, 2988.
- (20) Gupta, M. *Solid State Commun.* **1979**, *29*, 47.

- (21) Setoyama, D.; Matsunaga, J.; Muta, H.; Uno, M.; Yamanaka, S. *J. Alloys Compd.* **2004**, *385*, 156.
- (22) Fukai, Y.; *The Metal-Hydrogen System Basic Bulk Properties*; Springer Series in Material Science 21; Springer: Berlin, 1993.
- (23) McCarty, J. G.; Wise, H. *J. Catal.* **1979**, *57*, 406.
- (24) *Thermochemical Properties of Inorganic Substances*, Knacke, O., Kubaschewski, O., Hesselmann, K., Eds.; Springer: Berlin, 1991.
- (25) Blanter, M. S.; Golovin, I. S.; Granovskiy, E. B.; Sinning, H.-R. *J. Alloys Compd.* **2002**, *345*, 1.
- (26) Maeland, A. J. In *Hydrogen in Disordered and Amorphous Alloys*; Bambakidis, G., Bowmann, R. C., Jr., Eds.; Plenum: New York, 1986.
- (27) Kirchheim, R.; *Prog. Mater. Sci.* **1988**, *32*, 262.
- (28) Nijkamp, M. G.; Raaymakers, J. E. M. J.; van Dillen, A. J.; de Jong, K. P.; *Appl. Phys. A* **2001**, *72*, 619.
- (29) Chevallier, F.; Aymard, L.; Tarascon, J.-M. *J. Electrochem. Soc.* **2001**, *148*, A1216.
- (30) Texier-Mandoki, N.; Dentzer, J.; Piquero, T.; Saadallah, S.; David, P.; Vix-Guterl, C. *Carbon* **2004**, *42*, 2735.
- (31) Schlapbach, L.; Züttel, A.; Gröning, P.; Gröning, O.; Aepli, P. *Appl. Phys. A* **2001**, *72*, 245.
- (32) Schlapbach, L.; Züttel, A. *Nature* **2001**, *414*, 353.
- (33) San-Martin, A.; Manchester, F. D. *Bull. Alloy Phase Diagrams* **1987**, *8*, 30.
- (34) Yildirim, T.; Ciraci, S. *Phys. Rev. Lett.* **2005**, *94*, 175501.
- (35) Zhao, Y.; Kim, Y.-H.; Dillon, A. C.; Heben, M. J.; Zhang, S. B. *Phys. Rev. Lett.* **2005**, *94*, 155504.
- (36) Borchers, C.; Leonov, A. V.; Morozova, O. S. *J. Phys. Chem. B* **2002**, *106*, 1843.